Indian Journal of Pure & Applied Physics
Vol. 64, September 2026, pp. 998-1007
DOI: 10.56042/ijpap.v64i9.29904

A Multi-Wavelength NIR Spectroscopy Approach for Non-Invasive Blood Glucose Monitoring Using Artificial Neural Networks

Alok Kumar* & Mrutyunjay Rout

Electronics and Communication Engineering, National Institute of Technology Jamshedpur, Jharkhand 831 014, India

Received: 19th March 2026; accepted: 9th July 2026

Diabetes mellitus (DM) is a metabolic disorder characterized by elevated blood glucose levels. Diabetic patients must frequently monitor their blood glucose (BG) levels in order to estimate the insulin intake. Invasive methods are commonly used for blood glucose monitoring because they are extremely precise but require a blood sample, which is painful and increases the risk of infections. As an alternative, noninvasive techniques don't involve any damage to the skin, making them simple, painless, and practical for regular monitoring. A non-invasive glucose monitoring system based on near-infrared (NIR) spectroscopy is proposed. The system operates at three wavelengths (940 nm, 1050 nm, and 1300 nm) and utilizes both reflectance and transmittance signals for improved accuracy. An optoelectronic setup comprising light emitting diode (LED) and photodetectors is used to acquire NIR signals, which are then processed using an ATmega32 microcontroller. Data were collected from 62 human participants (37 male, 25 female) under fasting and postprandial conditions. An optimized artificial neural network (ANN) with 10 hidden layers achieved superior performance with an R^2 of 0.97 and MSE of 137.95, demonstrating strong potential for practical deployment. Clarke Error Grid analysis confirms that the majority of predictions fall within Zone A, indicating high clinical accuracy. The results validate the effectiveness of the proposed ANN-based approach for accurate, non-invasive, and real-time glucose monitoring.

Keywords: Blood glucose monitoring, Non-invasive measurement, Near-infrared (NIR) spectroscopy, Artificial neural networks (ANN), Clarke Error Grid (CEG)

1 Introduction

Diabetes is among the most prevalent and serious diseases impacting individuals globally. Diabetes mellitus is characterized by elevated blood sugar levels, a condition that impairs the body's ability to utilize energy. Generally, all forms of carbohydrates are converted into glucose, a simple sugar that powers the body's cells. The hormone insulin, found in the bloodstream, facilitates the conversion of blood glucose into stored energy. Insulin resistance, a shortage of insulin, or the body's overproduction of glucagon can all contribute to high blood glucose levels.

Insulin imbalance mainly caused by two primary factors: Type 1 diabetes, occurs when the immune system destroys insulin producing cells in the pancreas. Type 2 diabetes, which accounts for roughly 90 % of all diabetes cases, develops when the body is unable to produce enough insulin to keep blood sugar levels stable[1,2]. Higher blood sugar levels increase the risk of mortality by roughly 50 % compared to a healthy person, as they can lead to severe health complications including depression, heart disease, cognitive decline, vision problems, and kidney issues[3]. A diabetic person needs to consistently monitor their blood sugar levels and modify their diet and medication regimen as needed. Blood glucose monitoring methods can be categorized into three primary types: invasive, semi-invasive, and non-invasive. Invasive techniques are traditional methods that require a blood sample from the person. Although these methods are commonly used and produce dependable results, the frequent need for skin punctures can cause pain and discomfort while also increasing the chance of infection[4]. In contrast to capillary blood glucose tests, the semi-invasive approach evaluates glucose levels from interstitial or transdermal fluids. However, non-invasive techniques rely on analyzing physiological signals associated with glucose levels; they are painless, practical, and easy to use for continual monitoring.

In recent decades, many researchers have concentrated significant effort on noninvasive techniques for measuring blood glucose. Multiple non-invasive methods have been proposed to develop an accurate blood glucose monitoring system. Raman

*Corresponding author: E-mail: researchalok.51289@gmail.com

spectroscopy detect molecules by measuring the inelastic shift in the frequency of monochromatic light[5]. The installation requires considerable space and is not easily movable. The photoacoustic technique based on dual wavelength incorporating linearization was applied for glucose detection[6], while near-infrared photoacoustic spectroscopy method is employed for continuous glucose monitoring system[7]. A frequency-domain tissue spectrometer in the near-infrared was demonstrated to investigated the correlation between blood glucose and the reduced scattering coefficient of tissue[8]. The basis of the photo-acoustic method lies in detecting the ultrasonic waves that the molecule produces upon absorbing photon energy. When the energized molecules start to oscillate and the medium increases in size, an ultrasonic wave is produced. Molecules affect the light wave's polarity during the polarization process[9]. Due to the dextrorotatory characteristics of glucose, the linearly polarized light wave rotates in a clockwise direction as the concentration rises. The glucose-linked wavelength in the short-wavelength near-infrared region was identified using carbohydrate tolerance test (CTTs), Fourier transform spectrometer and an aqueous solution of sucrose, glucose and fructose[10-12]. The in vivo glucose measurement was investigated on dermal tissue spectra using near-infrared spectroscopy[13].A non-invasive sensor employing ultrasonic waves at the skin surface has been reported[14], but it has not been miniaturized to meet the criteria for a wearable sensor. A windowless resonator cell for non-invasive sensing has also been reported[15] describe a resonator cell without windows applied to the fingertip utilized in a non-invasive sensing system that relies on resonance-enhanced pulsed photoacoustic spectroscopy. Because of the intricate nature of this sensor system design, the cell must be enhanced further and incorporated into a portable device. Moreover, saliva has been used as a non-invasive approach for measuring glucose levels[16,17]. The glucose concentration is assessed via impedance spectroscopy across the skin as outlined in[18,19]. This approach will be ineffective because the electrical properties of sweat, skin, and saliva vary among individuals. The retina is employed for measuring glucose[20], demonstrating high accuracy, yet it is not appropriate for regular monitoring. Continuous glucose monitoring (CGM) or implantable systems are invasive technologies that require replacement because of their limited battery lifespan. Infrared (IR) spectroscopy, illustrating the interaction between optical radiation and materials, has been utilized for noninvasive detection of blood glucose level. In the near-infrared (NIR) range, water molecules in blood display partial transparency, allowing NIR signals to penetrate more deeply into body tissues than signals from the mid- and far-infrared ranges. Additionally, NIR-based devices are cost-effective, smaller, and less harmful than the laser techniques. Despite the many benefits of non-invasive devices, they are not used for diagnostic purposes as invasive methods provide greater accuracy.

In this study, the influences of blood glucose concentration on the transmittance and reflectance intensity are analyzed at three near-infrared wavelengths: 940 nm, 1050 nm, and 1300 nm. Photodetectors having high sensitivity at these wavelengths acquire NIR signals, which are then logged as discrete voltage values. The voltage values along with the glucometer reading are used to develop an artificial neural network (ANN) regression model. The device's medical precision is assessed utilizing a Clarke Error Grid (CEG) diagram. The key novelty of this study lies in the simultaneous utilization of transmittance (at 940 nm) and reflectance (at 940, 1050, and 1300 nm) signals within a single low-cost, microcontroller-based device, combined with an optimized ANN with 10 hidden layers. Unlike earlier research that rely on PLMR or simpler regression models, the proposed technique achieves a R^2 of 0.97 and RMSE of 11.74 mg/dL while preserving minimal hardware costs and portability.

2 Theoretical Background

NIR spectroscopy is based on the vibrational properties of molecular bonds at their resonance frequencies. When a light ray interacts with glucose molecules, it is both scattered and absorbed[21,22]. According to the Beer-Lambert law, the absorbance of light through any solution is proportional to the solution's concentration and the length of the light's travel. For reflectance spectroscopy, the attenuation of light propagating through a turbid medium is influenced by both absorption and scattering phenomena, which can be described using light transport theory, as expressed in Eq. (1).

$$I = I_0 \, e^{-\mu_{eff} \, L} \quad \text{... (1)}$$

where, I represent reflected light intensity, I_0 denotes the incident light intensity, and L is the optical path length of the tissue. The effective

attenuation coefficient (μ_{eff}) is the light attenuation within the tissue and is given by Eq. (2).

$$\mu_{eff} = \mu_a \sqrt{3\,\mu_a(\mu_a + \mu_s')} \quad \text{... (2)}$$

The absorption coefficient (μ_a) is the photon absorption within tissue per unit path length and μ_s' is the reduced scattering coefficient and it is given by Eq. (3) and Eq. (4) respectively.

$$\mu_a = 2.303 \in C \quad \text{... (3)}$$

$$\mu_s' = \mu_s\,(1-g) \quad \text{... (4)}$$

where, $\in$ represents the molar extinction coefficient, C denotes the concentration of tissue chromophores, μ_s is the scattering coefficient and g is the anisotropy factor of the medium. The variation in the refractive indices between extracellular fluid (ECF) and cellular membranes results in the scattering and absorption of light rays. The refractive indices for extracellular fluid (ECF) (η_{ecf}) and blood cells (η_{cell}) are estimated to be in the range of 1.348–1.352 and 1.350–1.460, respectively[8]. As the concentration of glucose rises, the difference between the refractive indices of ECF and cellular membranes diminishes due to an increase in η_{ecf}. This, in turn, leads to a reduction in scattering coefficients and optical pathways. Hence, Eq. (1) - (4) suggests that the intensity of reflected light reduces as the glucose concentration increases.

For transmittance spectroscopy, the attenuation of light intensity as it propagates through a medium is governed by the Beer–Lambert law, expressed in Eq. (5), which relates the reduction in transmitted intensity to the intrinsic absorption properties of the medium.

$$T = e^{-\tau} = 10^{-A} \quad \text{... (5)}$$

Or equivalently that

$$\tau = \sigma \int_0^t N(z)\,dz \quad \text{... (6)}$$

$$A = \varepsilon \int_0^t c(z)dz \quad \text{... (7)}$$

where, T represent the transmitted light intensity, l is the path length; N is the number density of the attenuating species in the material; σ is the attenuation cross section; ε is the molar attenuation coefficient; c is the molar concentration of the attenuating species in the material. In case of uniform attenuation these relation becomes as Eq. (8) - (9).

$$\tau = \sigma N l \quad \text{... (8)}$$

$$A = \varepsilon c l \quad \text{... (9)}$$

Thus, it can be concluded that the intensity of both reflected and transmitted light is inversely proportional to the molecular concentration. Therefore, at the resonant frequency of glucose molecules, the variation in the intensity of reflected and transmitted light waves can be used to estimate its concentration.

2.1 NIR Spectral Characteristics of Glucose Molecules

Infrared wavelength ranges from 600 nm to 25,000 nm and are classified into three regions: near-IR (700 nm-2500 nm), mid-IR (2500 nm-10,000 nm), and far-IR (10,000 nm- 25,000 nm). The near-IR is further classified as short NIR (600 nm-1300 nm) and long NIR (1300-2500 nm). The glucose molecule ($C_6\,H_{12}\,O_6$) has both single and double bonded atoms. The bonding atoms start vibrating at specific wavelengths through two processes: combination and overtone (stretching). The fundamental stretching of the glucose molecules is observed in the long-NIR region whereas its harmonics are observed in short-NIR region[11-13], shown in Table 1. The sharing of two or more fundamental frequencies in the mid- and far-NIR regions results in the vibration due to the combination process.

NIR spectroscopy is well-known for its basic idea and applicability. The interference caused by water content in the blood can be minimized by selecting an appropriate wavelength.

2.2 Wavelength selection

Near-infrared (NIR) light can be used to identify biological tissues based on wavelength absorption. In the long-NIR region, light wave absorption is higher, but the penetration depth is lower and gets

Table 1 — Fundamental vibration of bonds

Glucose bonds	Vibrational frequency overtones (nm)			
	Fundamental	1st	2nd	3rd
OH stretching	2860-3120	1410-1440	970	738
OH combinations	1920-2080	1100	840	--
CH stretching	3300-3470	1600-1800	1100-1230	910
CH combinations	2100-2352	--	--	--
CH_2 stretching	3460-3500	1720-1765	1215	930
CH_2 combinations	2310-2325	--	--	--

Note: The '–' symbol represents no data available

even smaller as the wavelength increases. The absorption in the short-NIR range is minimal, yet it penetrates human skin to a good depth of around 5 mm[23-25]. NIR equipment is easily accessible and less expensive than mid-infrared (MIR) and far-infrared (FIR) equipment. The informative bands in the short-NIR range for glucose detection were identified at 836 nm, 950 nm, 1040 nm, 1150 nm, 1280 nm, and 1395 nm[10-12], with a higher correlation coefficient.

In the proposed device, three NIR wavelengths were employed and obtained readings at four channels: transmittance signal at 940 nm; reflectance signal at 940 nm, 1050 nm, and 1300 nm, respectively. Despite the low absorption, a high correlation is observed at 940 nm wavelength, hence both transmittance and reflectance data are acquired at this wavelength. The NIR signals at wavelengths of 1050 nm and 1300 nm exhibit significant absorption and substantial attenuation in the transmitted wave; hence, reflectance spectroscopy data is obtained at these wavelengths. The combination of transmittance and reflectance spectroscopy was used to estimate the blood glucose level.

3 Materials and Methods

3.1 System Design and Implementation

The developed glucose monitoring device is based on optoelectronic circuit employing dual Near-Infrared (NIR) spectroscopy. The device has two probes that comprising four channels to obtain transmittance and reflectance readings. One probe is equipped with a 940 nm LED and two photodetectors, one photodetector is placed on the same side while other is placed just opposite side of the LED. In the other probe, a photodetector is placed between the 1050 nm and 1300 nm LEDs at a distance of 4 mm from each LEDs to obtain reflectance spectroscopy. The device is built on a printed circuit board, Fig. 1 illustrate the architecture of the device's configuration, and prototype is shown in Fig. 2. The probes are enclosed in a black box to minimize the interference due to external light sources. All components are integrated onto a Printed Circuit Board (PCB) and operate using a 12V DC power supply.

Two fingertips are inserted into the probes and kept steady for 40 seconds. Data is collected from each channel for ten seconds while others are turned off.

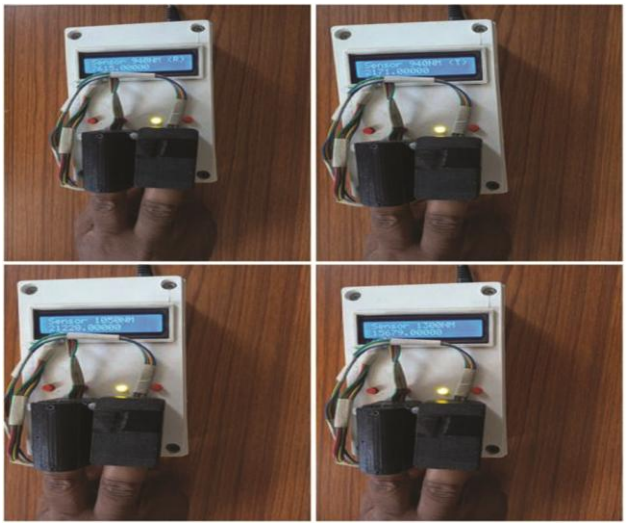

Fig. 2 — Prototype of the developed device

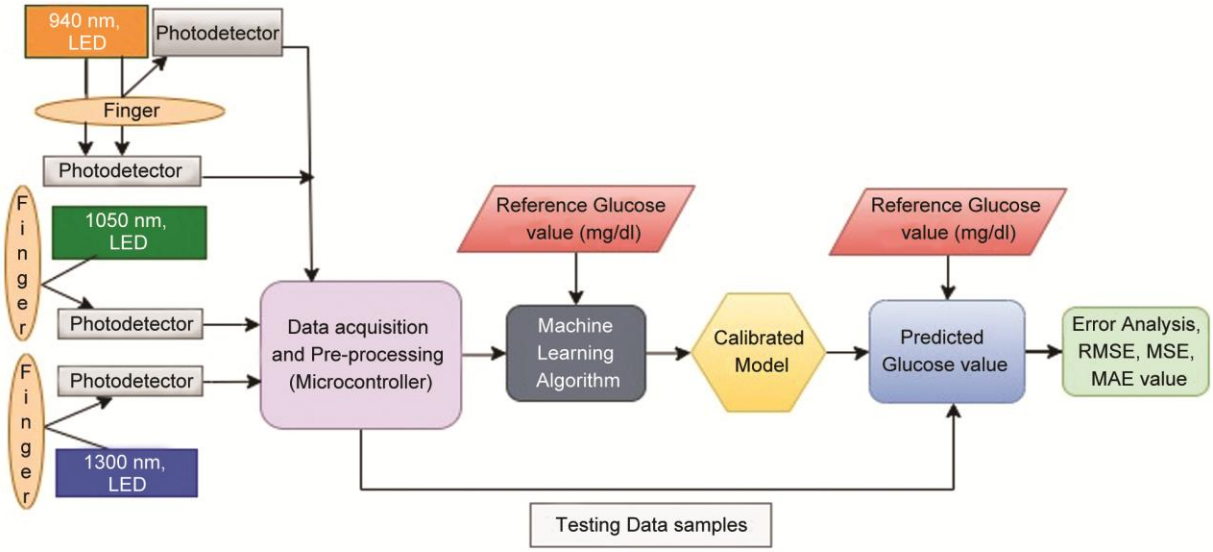

Fig. 1 — Architecture of the proposed device

A trans-impedance amplifier transforms the photodetector output current into voltage[26]. The microcontroller samples the voltage signals at a rate of 128 samples per second and represents each sample by 16 bits using external 32k-bit memory unit to minimize quantization error. To acquire the decimal voltage value, 1280 voltage samples are collected from each of the four channels over a duration of 10 seconds, and averaged to get the discrete voltage value. The block diagram shown in Fig. 3, depicts the process of transforming analog voltage into digital.

Simultaneously, a reading from an invasive glucometer (Control D) is acquired and utilized as the target value for the corresponding NIR signal reading. Table 2 presents a specification of the components used in the equipment.

3.2 Artificial Neural Network

Artificial Neural Networks (ANNs) are machine learning technique inspired by the structural and functional characteristics of the human brain. They consist of interconnected processing units, referred to as neurons, organized into multiple layers and linked through weighted connections[27-28], shown in Fig. 4. Each neuron receives input signals, performs a weighted aggregation, and produces an output through a nonlinear activation function. The network learns by adjusting these weights during the training process to optimize predictive performance.

3.3 Training and Optimization

The training of an ANN involves the iterative adjustment of synaptic weights and bias parameters to minimize the discrepancy between the predicted output and the corresponding ground truth. This optimization process is typically achieved using forward and backpropagation algorithm in conjunction with gradient-based learning methods. During forward propagation, the input data is passed sequentially through multiple layers Consider an input feature vector *x*, defined in Eq. (10), for each hidden neuron computes a weighted sum of its inputs with an added bias; thus, the net input to the j^{th} neuron[29,30] is given by Eq. (11).

$$x = [x_{1,} x_2, x_3, \ldots\ldots, x_n]^T \quad \ldots (10)$$

$$z_{j=\sum_{i=1}^{n} W_{ij}\, X_i} + b_j \quad \ldots (11)$$

Here, n is the number of input features, w_{ij} represents the synaptic weight from i^{th} input node to

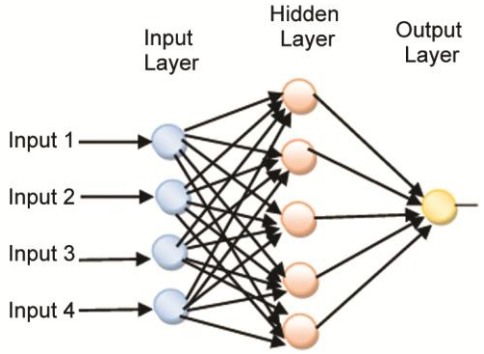

Fig. 4 — Architecture of the proposed multi-layer artificial neural network[28]

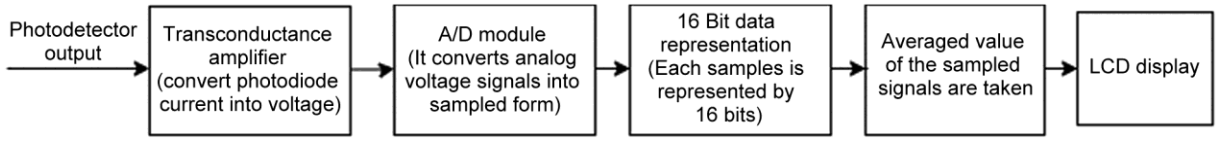

Fig. 3 — Data acquisition and signal processing

Table 2 — Specification of the hardware components

Components	Model name	Specifications
NIR LED	MTE5010-525-IR	Peak Wavelength=1050 nm, Forward voltage=1.5 V Radiant Power=4 mW
	MTE1300N5	Peak Wavelength=1300 nm, Forward voltage=1.05 V Radiant Power=120 mW
Photo-detector	MTPD1346D-100	Sensitivity range=600nm-1750nm, Dark current=2 µA Breakdown voltage=3v
Microcontroller	ATmega32	40 pin DIP, 8 channels, 10-bit resolution ADC RAM= 2Kbytes, 32k byte programmable memory
Invasive Glucometer	Control D	Minimum Blood Sample: 0.5 µL Measuring Time: 5 second
Environmental conditions	Room temperature (22–25°C), Relative humidity (40–60 %), Dark enclosure for each probe to eliminate ambient light interference	

the j^{th} neuron, b_j denotes the bias, and Z_j is the aggregated input signal. The nonlinear activation functions applied to neurons, enabling the learning of complex patterns and is given by Eq. (12), thus the forward propagation for the l^{th} layer is given Eq. (13).

$$a_j = f(z_j) \quad \text{... (12)}$$

$$a^{(l)} = f(W^{(l)}\, a^{(l-1)} + b^{(l)}) \quad \text{... (13)}$$

This process continues across successive layers until the final layer generates the predicted output ŷ. The network's performance is evaluated using the Mean Squared Error (MSE) loss function[30], which quantifies the discrepancy between the predicted output ŷ and the target value $\bar{y}_k$ and given by Eq. (14).

$$MSE = \frac{1}{N}\sum_{k=1}^{N}(\hat{y}_k - \bar{y}_k)^2 \quad \text{... (14)}$$

The optimization of ANN parameters is performed using the backpropagation algorithm, which computes gradients of the loss function with respect to network weights and biases using the chain rule of calculus. The weight and bias between the i^{th} input neuron and the j^{th} neuron are updated by Eq. (15) and Eq. (16), to minimize the loss function.

$$w_{ij}^{(t+1)} = w_{ij}^{(t)} - \eta \frac{\partial E}{\partial w_{ij}} \quad \text{... (15)}$$

$$b_j^{(t+1)} = b_j^{(t)} - \eta \frac{\partial E}{\partial b_j} \quad \text{... (16)}$$

where η denotes the learning rate controlling the step size of the update. Through repeated iterations over the training dataset, the weights and biases are progressively adjusted to minimize the loss function, enabling the neural network to learn an optimal mapping between input features and target outputs.

3.4 Performance Evaluation Metrics

The R-squared (R^2) value is used to assess how accurately the model fits the data set[30] The higher the R^2 value, the more closely the model fits the data set Eq. (17).

$$R^2 = 1 - \frac{SSR}{SST} = 1 - \frac{\sum_{i=1}^{n}(y_i - \hat{y}_i)^2}{\sum_{i=1}^{n}(y_i - \bar{y})^2} \quad \text{... (17)}$$

where y_i is the i^{th} instance of actual value *Y*, sum of square errors (SSR) with the best fit line, and the sum of errors (SST) with respect to the average fit of the line. The model's performance is examined in terms root mean square error (RMSE) values[30], calculated using Eq. (18). The RMSE is the standard deviation of the error around the regression plane.

$$RMSE = \sqrt{\frac{1}{n}|y_i - \hat{y}_i\,|^2} \quad \text{... (18)}$$

4 Results and Discussion

The labeled dataset comprises discrete voltage readings obtained from three near-infrared (NIR) wavelengths across four sensing channels, along with corresponding invasive glucometer measurements. Data were collected from 62 human participants under both fasting and postprandial conditions, in accordance with established medical safety protocols. The details of the individuals are given in Table 3.

A total of 320 samples were collected and partitioned into training (256 samples, 80 %), validation (32 samples, 10 %), and testing (32 samples, 10 %) datasets. The neural network was trained using Levenberg-Marquardt backpropagation technique with varying numbers of hidden layers. The performance of the models was evaluated using the coefficient of determination (R^2) and mean squared error (MSE), as presented in Table 4.

The results demonstrate that with the increase in the number of hidden layers the performance of the model increases. The ANN model with 10 hidden layers provides the most favorable performance with an R^2 of 0.9706 and the lowest MSE of 137.95. Further increasing the hidden layers has significant

Table 3 — Characteristics of individuals

Gender-Age(years)	Age (years)	Normal	Pre-diabetic	Diabetic	Total
Male	21-65	16	12	9	37
Female	20-58	12	6	7	25

Table 4 — Performance of ANN with varying hidden layers

Hidden layers	R2	MSE
1	0.936	337.305
2	0.948	251.788
3	0.956	224.824
4	0.968	200.657
5	0.968	191.102
6	0.964	180.780
7	0.968	179.266
8	0.968	193.028
9	0.964	188.489
10	0.970	137.948
11	0.970	175.607
12	0.970	166.309

effect on the R^2 value but exhibit increased MSE value, suggesting reduced prediction stability and possible overfitting. Several conventional machine learning-based computation models along with the proposed ANN model with 10 hidden layers, examined to get optimized model for precise glucose measurement, shown in Table 5. The simulation of all the regression models and proposed optimized ANN models was performed on the MATLAB application tool.

The results indicate that the deep learning approach effectively captures the nonlinear relationship between NIR sensor signals and blood glucose concentration. The traditional regression techniques exhibit lower predictive accuracy and relatively higher error metrics as compared to the proposed ANN model. Thus, an optimized ANN model with 10 hidden layers adopted for device implementation due to its improved predictive accuracy and robustness. The correlation between predicted and target blood glucose concentration for the training, validation and testing data set is shown in Fig. 5, that shows a strong linear correlation and minimal deviation from the ideal fit line. Figure 6 (a) presents the training performance trajectory, demonstrating rapid convergence and stable learning behavior. Figure 6 (b) displays the error histogram, revealing a symmetric distribution centered near zero with minimal outliers, further confirming the model's prediction reliability.

The bar plot comparison between the predicted and reference values for the validation and testing data set is shown in Fig. 7.

Table 5 — Statistical analysis of different regression models

Regression Models	R^2	RMSE	MSE
Linear Regression	0.52	1337.32	1.7884e06
Stepwise Linear	0.46	1425.27	2.031e06
Fine tree	0.56	1274.71	1.6249e06
Medium tree	0.55	1289.56	1.6628e06
Linear SVM	0.52	1345.38	1.8099e06
Coarse Gaussian SVM	0.53	1328.62	1.7653e06
Exponential Gaussian process regression	0.65	1138	1.295e06
PLMR	0.84	22.43	298.70
Proposed (ANN model with 10 Hidden layers)	97.0	11.74	1.3793e02

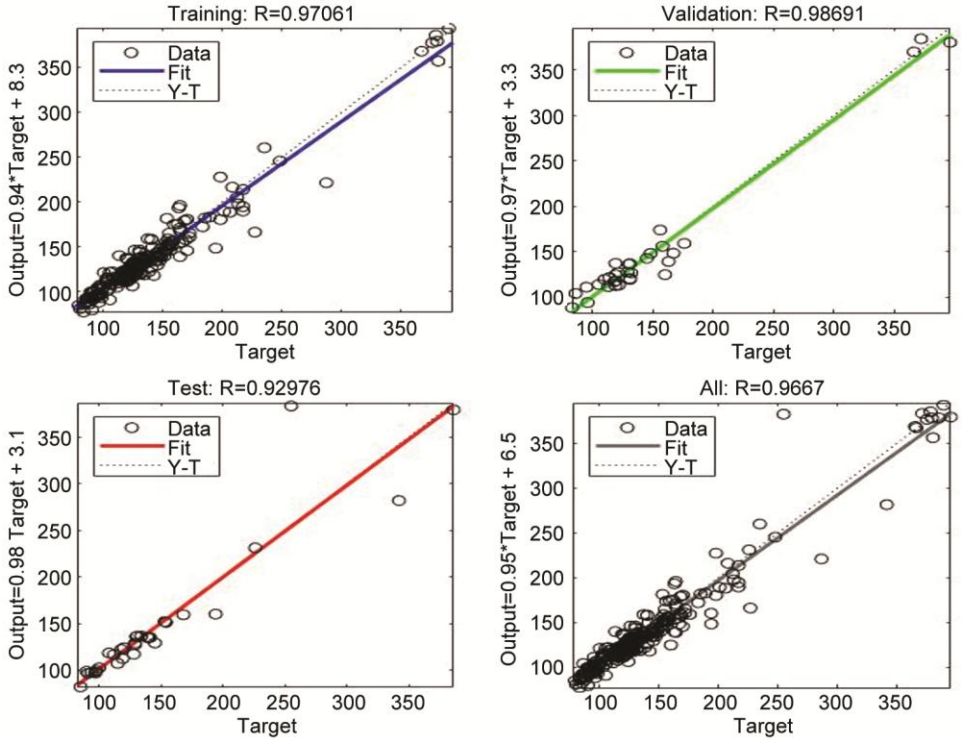

Fig. 5 — Correlation plot between predicted and target glucose concentration for training, validation and testing data set

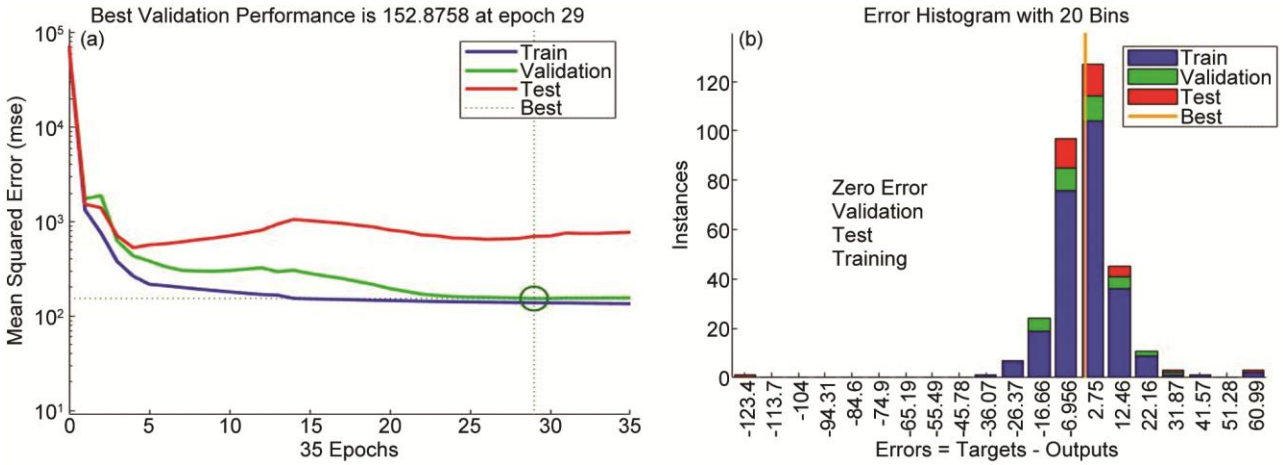

Fig. 6 — Training performance metrics for the optimized ANN model (a) Training performance convergence; and (b) Distribution of prediction errors

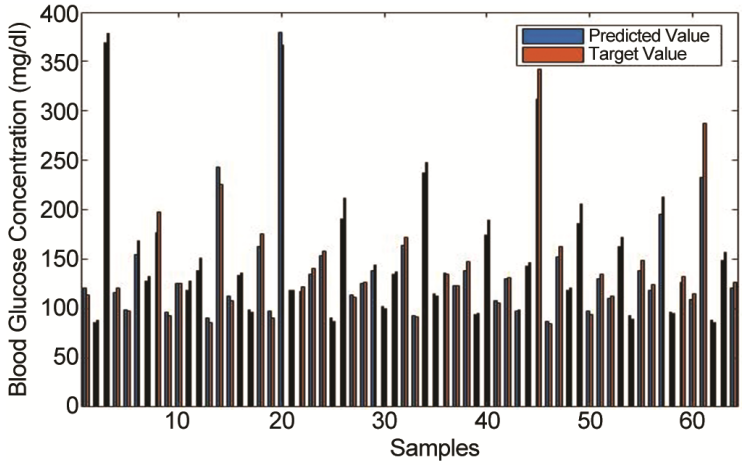

Fig. 7 — Bar plot comparison of predicted and target glucose values for testing and validation dataset

4.1 Clarke Error Grid

The Clarke error grid (CEG) plot is used to analyze the device's clinical accuracy, which classifies prediction errors into clinically relevant risk zones. Zone A corresponds to clinically accurate predictions, while Zone B includes errors that have minimal clinical impact. In contrast, Zones C to E indicate increasing levels of clinical inaccuracy and potential risk. The Clarke error grid plot for training testing dataset, covering a glucose range of 79–390 mg/dL is shown in Fig. 8. It shows most of the predicted glucose values fall within region A, indicating the proposed device offers reliable glucose estimation and holds strong potential for practical clinical use. Which is clinically acceptable for glucose measurement devices.

The performance of the device is also compared with the previous non-invasive works as shown in Table 6.

The result show that the previous studies reported R^2 values ranging between 0.74 and 0.94, and RMSE values ranges from 7.5 mg/dL to 18.88 mg/dL. The data were obtained at the same wavelengths, and an optimized PLMR algorithm were and achieved RMSE of 17.28 mg/dL and an R^2 of 0.9224, showing decent but not outstanding performance[1]. In contrast, the proposed system achieved a noticeably better RMSE of 11.74 mg/dL and an R^2 of around 0.97, all while keeping device costs low.

Despite promising results, the proposed system has several limitations. Motion artifacts during the 40-second measurement period can introduce voltage fluctuations; future work will implement real-time motion detection and rejection. Variations in skin hydration, temperature, and pigmentation across individuals may affect NIR light penetration and scattering. Additionally, sensor placement on different

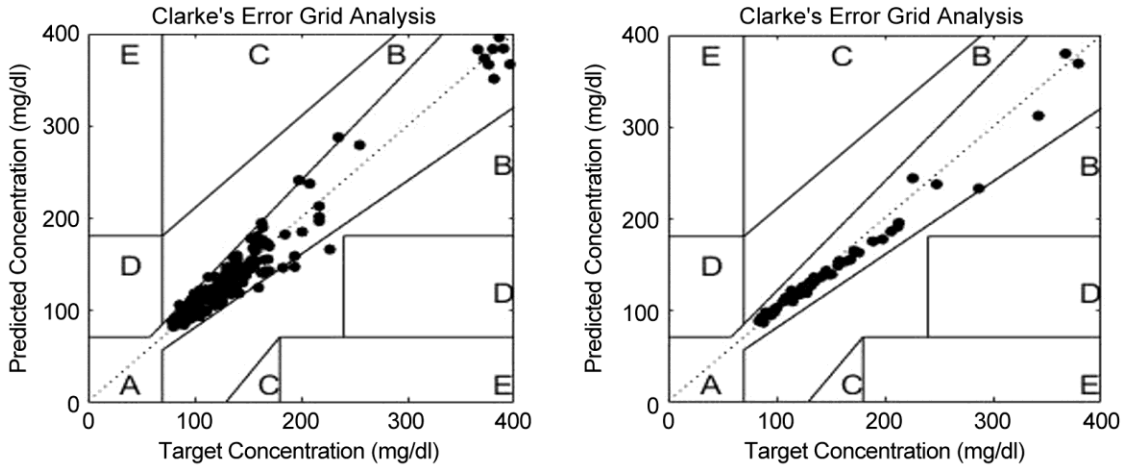

Fig. 8 — Clarke Error grid plot for (a) Training data sets; and (b) Testing data sets

Table 6 — Statistical comparison of previous non-invasive works

Research works	Wavelength (nm)	Spectroscopy	sample	RMSE (mg/dL)	R^2	Device cost
[1]	940,1050,1300	Transmittance Reflectance	Blood	17.2833	0.9224	low
[4]	940	Reflectance	Blood	18.88	--	low
[14]	940,1300	Transmittance and Reflectance	Blood (capillary)	7.5	0.90	high
[21]	1550	Transmittance	Blood	--	0.74	low
[22]	940,1300	Transmittance and Reflectance	Blood (capillary and serum)	13.57	0.94	high
Proposed	940,1050,1300	Transmittance Reflectance	Blood	11.74	97.0	low

fingertips or positions on the same finger may produce slightly different readings. Tissue heterogeneity (e.g., bone, fat, muscle) also influences optical path length. These factors will be addressed in future designs through adaptive calibration and multi-site sensing.

5 Conclusion

A non-invasive glucose monitoring device based on multi-wavelength NIR spectroscopy and deep learning was developed and experimentally validated. The concept of vibrational characteristics of glucose molecules under NIR light is used to estimate their concentration. The device utilizes transmittance signals at 940 nm along with reflectance signals at 940 nm, 1050 nm, and 1300 nm to capture glucose-related optical variations. These variations are converted into discrete voltage signals using a custom-designed optoelectronic circuit. An optimized ANN-based regression model with 10 hidden layers was implemented to estimate glucose levels, achieving high accuracy with an R^2 of approximately 0.97 and an RMSE of 11.74 mg/dL. The device is also validated on Clarke Error Grid Plot and demonstrates the feasibility of using a non-invasive blood glucose measurement technique. In addition to its accuracy, the device is low-cost, portable, and painless, making it well-suited for continuous glucose monitoring. Future work will focus on expanding the dataset, improving the robustness of the model, and integrating the system into wearable healthcare solutions.

References

1 Kumar A & Rout M, *Ind J Pure & Appl Phys (IJPAP)*, 63 (9) (2025) 803.
2 Haxha S & Jhoja J, IEEE *Photon J*, 8 (6) (2016) 1.
3 Dorsaf G, Yacine M & Khaled N, *Curr Res Diabetes & Obes J*, 11 (1) (2019) 1.
4 Yang X, *et al.*, *Conference on Lasers and Electro-Optics (CLEO) IEEE*, JW2A (2012) 105.
5 Tajima T, *et al.*, *IEEE Sensor J*, 17 (16) (2017) 5079.
6 Jain P, Joshi A M & Mohanty S P, *Biomed Signal Process Control*, 79 (2023) 104172.
7 Ahmed T M, Mahyoob M & Mohamed K A, *8th International Conference on Signal Processing and Information Security (ICSPIS)*, IEEE, 2025.
8 Maier J S, *et al.*, *Opt Lett*, 19 (24) (1994) 2062.
9 Khan M S, Varshney G & Giri P, *IEEE Trans NanoBiosci*, 20 (4) (2021) 488.
10 Uwadaira Y, *et al*., *Biomed Opt Express*, 7 (7) (2016) 2729.
11 Zhang W, *et al*., *Biomed Opt Express*, 4 (6) (2013) 789.
12 Yang W, *et al*., *Aip Adv*, 8 (3) (2018) 035216.

13 Golic M, Walsh K & Lawson P, *Appl spectrosc*, 57 (2) (2003) 139.
14 Li, D, *et al*., *Opt Diagnos Sensing VII*, 6445 (2007) 64450I.
15 Pleitez M A, *et al*., *Rev Sci Instrum*, 84 (8) (2013) 084901.
16 Prasad, M S, *et al*., *IEEE Sensors J*, 18 (13) (2018) 5203.
17 Singh A K & Jha S K, *IEEE Sensors J*, 19 (18) (2019) 8332.
18 Dai T & Adler A, *IEEE Trans Instrument Measure*, 58 (11) (2009) 3831.
19 Song K, *et al*., *IEEE J solid-state circuit*, 50 (4) (2015) 1025.
20 De P, Ramos L, *et al*., *J Biomed Opt*, 21 (8) (2016) 086007.
21 Maruo K, *et al*., *IEEE J Sel Top Quant Electr*, 9 (2) (2003) 322.
22 Joshi, A M, *et al*., *IEEE Trans Consumer Electr*, 66 (4) (2020) 327.
23 Padalkar M V & Pleshko N, *Analyst*, 140 (7) (2015) 2093.
24 Huang M, *et al*., *Sensors*, 16 (4) (2016) 441.
25 Daarani P & Kavithamani A, *Int J Latest Trends Eng Technol*, 8 (3) (2017) 141.
26 Saleh G, *et al*., *J Med Eng Technol*, 42 (2) (2018) 140.
27 Thorat M, Pandit S & Balote S, *Asian J Converg Technol*, 8 (3) (2022) 12.
28 Bhasin P & Vaishali, *Int J Eng Res Technol*, 5 (10) (2017) 1.
29 Kim G & Bak Y, *Electr*, 14 (23) (2025) 4718.
30 Izonin I, *et al*., *Technol*, 12 (7) (2024) 112.